JOINT EUROPEAN TORUS

JET–P(90)01

D. Pasini, M. Mattioli, A.W. Edward, R. Gianella, R.D. Gill, N. Hawkes,
G. Magyar, B. Saoutic, Z. Wang and JET Team

Impurity Transport in JET Using Laser-injected High-Z Impurities in Ohmic and RF Heated Plasmas

Impurity Transport in JET Using Laser-injected High-Z Impurities in Ohmic and RF Heated Plasmas

D. Pasini, M. Mattioli[1], A.W. Edward, R. Gianella, R.D. Gill, N. Hawkes[2], G. Magyar, B. Saoutic[1], Z. Wang[3] and JET Team*

JET-Joint Undertaking, Culham Science Centre, OX14 3DB, Abingdon, UK

[1]EURATOM-CEA Association, Cadarache, France
[2]EURATOM-UKAEA Association, Culham Laboratory, United Kingdom
[3]Southwestern Institute of Physics, Leshan Sichuan, PRC
[2]EURATOM-IPP Association, Garching, FRG
** See Appendix 1*

Preprint of Paper to be submitted for publication in
Nuclear Fusion

ABSTRACT.

Small,quantities of high-Z impurities have been injected into JET plasmas and their progression was followed with good spatial and temporal resolution using two soft X-ray cameras. The results show that the transport of impurities is much slower in the central region of the plasma than in the outside and that it is greatly enhanced during sawtooth crashes. Simulation of the evolution of the emissivity profiles using an impurity transport code yielded values for the radially dependent transport coefficients and in particular these values have been compared in the cases of ohmically heated and RF heated plasmas.

1. INTRODUCTION

Transient perturbation methods are the most appropriate to study particle transport in tokamaks. Information is derived from observations of local variations of the electron density n_e and on the detection of emission from impurity ions located in different spatial regions. Usually an interpretation is made in terms of a diffusion coefficient D and an inward convection velocity V. Typical numerical values are in the range of 1 m^2/s and of a few m/s respectively and are generally larger than the predictions of the neoclassical theory.

In the Joint European Torus (JET) various transient methods have been used to study electron transport in the plasma interior [1,2] and impurity transport has been measured following either accidental metal injection [3] or impurities injected by laser blow-off [4]. The latter is undoubtedly the best way to study impurity transport. Both the injection time and the amount of injected material can be controlled to study a chosen phase of the discharge with a minimum perturbation of the plasma parameters. Furthermore the source is of very short duration thus providing an experimentally more direct measure of impurity transport. In most studies using this technique the analysis is based on the detection and simulation of line brightnesses using an impurity transport code [5-8]. The central ion brightness decay times are identified with the impurity confinement times and are often used to compare different discharge regimes [9].

Impurity transport can also be studied using X-ray diode arrays which offer the advantage of high spatial and temporal resolution (a few centimetres and a few tens of microseconds respectively) with the inconvenience that all the atomic species contribute to the detected signal. They are nevertheless advantageous in case of laser blow-off injection since by signal subtraction it is possible to isolate the contribution of the injected element. Also, reliable simulation is possible, since then the soft X-ray signal is caused by the K_α- or L-lines and by the free-bound and free-free continua. The first time- and space-resolved studies on injected impurities were performed on Alcator-C [10,11]. Soft X-ray signals from injected Si were simulated by assuming flattening of the impurity ion density profile during sawteeth. Thus it was possible to explain the inverted sawtooth during the inflow part of the injected element when the injected ion density profile was hollow.

More detailed quantitative studies have been possible on PLT [12] concerning the inverted sawtooth observed with the soft X-ray diodes following Al injection. It was concluded that impurities are prevented from reaching the centre during the quiescent phase of the sawtooth, that is the transport coefficients are very small inside the q=1 region, and that the internal disruption leads to a very high enhancement of the diffusion coefficient in the central region.

This paper presents the results of laser blow-off injection experiments in Ohmic and RF heated JET plasmas. The progression of the impurities into the plasma was followed using two soft X-ray cameras permitting tomographic reconstruction of the X-ray emission. The large plasma dimension allowed impurity transport to be measured with high spatial and temporal resolution. The results show clearly the reduction of impurity transport in the central region of the plasma and the rapid modification of the impurity distribution which occurs during a sawtooth crash. Detailed transport simulations have been possible during the quiescent phases, i.e. between internal disruptions, to determine the values of the radially dependent transport coefficients.

Section 2 contains a description of the experimental conditions and the experimental results. The impurity transport model and the results of the simulations are presented in Sections 3 and 4, respectively. Section 5 contains a summary of the results which are compared to neoclassical predictions and electron transport measurements.

2. EXPERIMENTS

2.1 Experimental Conditions and Diagnostics

JET is a D-shaped large tokamak with major radius R_o = 2.96 m, minor radius a = 1.25 m, nominal toroidal field B_T = 3.4 T, plasma current I_p up to 7 MA and plasma elongation = 1.6. The JET plasma is quite advantageous for studying quiescent impurity transport, since the sawtooth period in Ohmic plasmas is increased with respect to smaller devices up to 50-100 ms [13]. Moreover, in ion-cyclotron radio frequency (RF)-heated plasmas the plasma can undergo a transition into a new regime with the sawtooth instability suppressed for long periods

(up to 5 sec), but with much larger T_e drop at the crash (the so-called monster sawtooth) [14].

Metallic impurities have been injected into JET plasma by laser blow-off to study transport phenomena. The amount of injected impurities was kept sufficiently low to avoid perturbing any plasma parameters apart from radiation. This corresponded to a concentration of 0.01 to 0.05% of n_e i.e. a few 10^{18} atoms. The laser blow-off system [15] uses a single pulse (~2J, 20 ns) from a Ruby laser system. The target chamber is attached to the bottom of the vessel and the injection point is approximately 2 m from the plasma boundary. The injected neutral particles have energies of the order of a few eV and reach the plasma boundary in less than 1 ms. The atoms are ionised at the plasma edge and spread out rapidly along the field lines with a toroidal velocity in the 10^4 m/s range. At the same time due to collisions or turbulence, the ions move slowly radially inwards with typical velocities of 1-10 m/s.

The progression of the impurities into the plasma is followed with good spatial and temporal resolution using two soft X-ray imaging cameras (100 detectors total) covered with 250 μm Be filters, which view the same poloidal cross section of the plasma in orthogonal directions [16]. This allows the use of a tomographic reconstruction method [17] to obtain the local spatial distribution of X-ray emission as a function of time. The ultimate time resolution is 5 μs and the limiting spatial resolution, determined by the chord spacings and the reconstruction technique, is roughly 0.1 m. This means that any emission feature which has spatial dimension smaller than 0.1 m will be downgraded to this limiting resolution. An X-ray pulse-height spectrometer [18] equipped with an X-ray filter similar to the one used on the X-ray cameras allows the energy resolution of the radiation measured with the camera system and the identification of the extra radiation due to the injected impurity. VUV spectrometers are used to measure the line brightnesses of peripheral ions providing information on the impurity source function. The profiles of electron density and electron temperature which are needed for the transport simulations are obtained from interferometric measurements [19] and from absolutely measured values of the electron cyclotron emission (ECE) [20].

2.2 Experimental Results

Various types of impurities have been injected predominantly into Ohmic discharges although a number of RF, NBI and combined heating discharges were explored. In this paper we present the results of two particular injection experiments where Ni was injected into a 3 MA ohmically heated deuterium discharge and Mo into a 3 MA deuterium plasma heated with 6 MW of RF. These two examples have been selected because they provide a comparison of impurity transport for two different discharge regimes with very different sawtooth periods. In the Ohmic case the sawtooth period (~ 70 ms) was much less than the impurity confinement time (~ 310 ms) while in the RF heated case the sawtooth period (~ 650 ms) was greater than the impurity confinement time (135 ms). The Z values of the impurities were not a significant factor in this comparison since for three consecutive ohmic discharges the time evolution of the soft X-ray signal was the same when using either Ti, Fe or Mo.

2.2.1 Ni injection into a 3 MA ohmically heated limiter discharge

Ni is injected at 10.990 s (blow-off time) during the flat top of a 3 MA limiter discharge with a central electron density of 2.0×10^{-19} m^{-3} and a central electron temperature of 4000 eV (see Fig.1). The background gas is D_2 and Z_{eff} = 5 due to strong carbon contamination. The quantity of injected particles is small corresponding to a concentration of ~ 5×10^{-4} of the electron density and as shown in Fig.1 this does not disturb in any noticeable way the plasma current, the electron density or the electron temperature. However, the signature of Ni injection clearly shows on the bolometer trace measuring the total radiated power and on the central chord soft X-ray intensity signal (E ≥ 2 keV). Figure 2 shows the PHA spectrum before and after nickel injection. The most noticeable difference is the appearance around 8 keV of a peak due to K_α line radiation from predominantly He-like Ni ions. Calculations show that the extra radiation measured by the X-ray cameras is ~50% line radiation and 50% continuum radiation.

Figure 3 shows an expanded view of the central chord soft X-ray intensity around the time of Ni injection. It represents the contribution from injected Ni alone, the background level having been subtracted. This can be done as the background emission is nearly

constant apart from the sawtooth activity which represents only a minor perturbation compared with the extra emission due to the injected impurities. As the impurities propagate inwards they enter regions of higher electron density and higher electron temperature and the intensity of the signal grows. At the time of the maximum of the X-ray signal the impurity concentration is near its maximum in the plasma centre. The signal then starts to decay as the impurities continuously leak out. During the rising phase of the signal we observe that the sawteeth are inverted. This implies an inward flow of impurities into the central region at the time of a sawtooth crash. Similarly during the decay phase of the signal the fall in intensity at the time of each sawtooth crash is greater than can be accounted for by the temperature drop alone. This implies an outward flow of impurities from the central region during sawtooth crashes.

Figure 4 shows tomographic reconstructions of the X-ray emissivity distributions (background emission subtracted) for the times indicated by the dashed lines in Fig.3 and corresponding to 50, 140 and 200 ms after injection during the rising phase of the signal and 340, 450 and 610 ms during the decaying phase of the signal. Since the X-ray distribution is roughly poloidally symmetric, to follow the progression of the impurities as a function of time it is sufficient to display the evolution of the X-ray emissivity distribution along a horizontal central chord as shown in Fig.5. This covers the period of time starting immediately after the first sawtooth crash following injection and ending just before the maximum of the X-ray signal (see Fig.3). The times t_1 and t_2 indicate the two sawtooth crashes which occur during that period.

The data of Fig.5 show that during the quiescent phase of the first sawtooth an increasingly hollow emissivity distribution develops as the impurities pile up approximately 0.4 m from the plasma centre, just outside the sawtooth inversion radius at 0.35 m. During the sawtooth crash, which lasts ~ 100 μs, a significant redistribution of the impurities occurs which causes the peak of the X-ray distribution to move inwards by 0.13 m across the inversion radius. A simulation of the emissivity profiles shows that the impurity density is larger at the new peak position after the sawtooth crash than it was at the previous peak position before the crash. This means that the convection must be

important during this inward movement. During the quiescent phase from t_1 to t_2 the X-ray profile remains hollow. It is only at the next sawtooth crash that the impurities finally fill up the central region. The movement of the impurities during an internal disruption is clearly more complicated than can be explained by a simple flattening of the impurity distribution.

The build up of a hollow emissivity distribution and the slow evolution of the emissivity profile inside the central region between sawtooth crashes clearly indicates that impurity transport is much smaller in the central region of the plasma than outside of it. Other observations made after injecting Mo in a plasma of similar conditions confirm the overall behaviour seen with Ni injection. The quantitative analysis of these results is presented in Section 4.

2.2.2 Mo injection into a 3 MA RF heated limiter discharge

Figure 6 shows the time evolution of a central chord soft X-ray signal and the central electron temperature for a 3 MA limiter discharge with 6 MW of RF heating. The background gas is D_2 and $Z_{eff} = 3$. Additional heating starts at 5 s and the power is gradually ramped up reaching a maximum of 6 MW at 6.7 s. As well as causing the central electron temperature to increase from 4 to 9 keV and the central electron density from 2.1 to 2.9×10^{19} m^{-3}, the sawtooth period is increased from ~ 40 ms up to 650 ms. Mo was injected into this discharge at 7.387 s when the heating power was at its maximum and during the longest sawtooth, 133 ms before it crashed. The extra emission measured by the X-ray diodes is roughly accounted for by one third to continuum radiation and two thirds to L-lines radiation between 2.6 and 3.3 keV from Li-like to Ne-like ionisation stages.

In the case of RF heating the sawtooth activity represents a very important perturbation of the X-ray signal compared with the extra emission due to the injected impurities. To correct properly for the changing background emission, the X-ray signal, free of Mo impurity radiation and starting 133 ms before the crash at 8.197 s, was subtracted from the X-ray signal starting 133 ms before the sawtooth crash at 7.520 s. Fig.7 shows the central chord soft X-ray intensity around the time of Mo injection with the background emission subtracted.

As in the Ohmic case the sawtooth is inverted indicating an inward flow of impurities at the time of the crash. Comparing this figure with Fig.3 it is clear that the Mo impurity transport was faster for these plasma conditions as the signal peaks and decays more rapidly. The characteristic decay time as determined from Fig.3 and Fig.7 is 310 ms in the ohmic case and 135 ms in the RF heated case. The X-ray data of several other discharges have been looked at and systematically indicate faster transport when additional heating is present.

Figure 8 shows the time evolution of the X-ray emissivity distribution along a horizontal central chord after Mo injection. Up to the sawtooth crash the emission becomes more and more hollow as the impurities pile up at a location roughly 0.35 m from the plasma centre inside the sawtooth inversion radius at 0.42 m. As in the ohmic case this clearly indicates that impurity transport is much smaller in the central region of the plasma. During the sawtooth crash the transport is dramatically enhanced leading to the immediate filling of the central region of the plasma. Following the crash the rapid loss of particles on the outside causes a continuous narrowing of the emissivity profiles.

The movement of the impurities during a sawtooth crash can be determined from reconstructions of the X-ray distribution during this phase. Figure 9 shows a comparison between the normal sawtooth crash at 8.197 s and the sawtooth crash at 7.520 s when impurities are present. In both cases the total X-ray emission is shown (i.e. no background subtraction), the time resolution is 5 μs and the reconstruction covers a period of 300 μs. The behaviour during the sawtooth at 8.197 s (Fig.9A) has already been observed many times [21]. The hot central region moves rapidly outwards until it reaches r/a ~ 0.3 while colder plasma fills the interior space. This movement takes approximately 50 μs. The emission from the hot spot then decays rapidly on a time-scale of 100 μs spreading out poloidally on the surface where it has been squeezed out. For the sawtooth crash at 7.520 s (Fig.9B) the initial X-ray distribution is slightly hollow because Mo impurities have accumulated near r = 0.35 m. The drop in the central emission which was observed in the former case when the hot core moved out (the displacement is in the opposite direction here) is not observed since the colder plasma which is dragged in has roughly the same emissivity

because of a higher impurity content. This clearly indicates that the impurities are moving in on the same time scale as the crash itself.

3. NUMERICAL MODEL

The transport simulations presented in the next section have been performed using the impurity transport code developed on TFR [22]. The code calculates, in cylindrical geometry, the solution of the following set of partial differential equations for the impurity ions:

$$\frac{\partial n_Z}{\partial t} = -\frac{1}{r}\left(\frac{\partial}{\partial r}(r\Gamma_Z)\right) + n_e\left[n_{Z-1}\,S_{Z-1} - n_Z S_Z + n_{Z+1}\,\alpha^R_{Z+1} - n_Z\,\alpha^R_Z\right]$$
$$+ n_D\left[n_{Z+1}\,\alpha^{CX}_{Z+1} - n_Z\,\alpha^{CX}_Z\right] - \frac{n_Z}{\tau_{//}} \qquad Z = 1,\ldots,Z_N \quad , \tag{1}$$

where Γ_Z is the radial particle flux density (positive when directed outwards) of the ions of charge Z, nuclear charge Z_N and density n_Z. S_Z, α^R_Z and α^{CX}_Z are the ionisation rate coefficients, the radiative plus dielectronic recombination rate coefficients and the charge exchange recombination rate coefficients, respectively, for the ions of charge Z. $\tau_{//}$ is the impurity confinement time for particle transport along the field lines.

Input parameters for the code are the $n_e(r)$ and $T_e(r)$ profiles. S_Z, α^R_Z and α^{CX}_Z are functions of the radius r because of their electron temperature dependence. Charge exchange recombination has been neglected since the numerical simulations essentially involve the central plasma where the n_D values are small.

A separate equation is included to describe the ionisation of the neutral injected atoms of density n_o. The boundary condition for this equation at the last mesh radius r=a is written as:

$$\Gamma_o = n_o(a)\,V_o = \Gamma_{ext} + R\,\textstyle\sum_Z \Gamma_Z(a) \quad . \tag{2}$$

That is Γ_o, the total neutral particle flux density entering into the plasma with directed velocity V_o is set equal to the sum of an external flux density Γ_{ext} and a recycling flux density. The latter is the total outward flux density $\sum_Z \Gamma_Z(a)$ at the last mesh recycled with recycling coefficient R. The

radial flux density Γ_Z is described using both diffusive and convective terms:

$$\Gamma_Z(r) = - D(r) \frac{\partial n_Z}{\partial r} - V(r)\, n_Z \quad . \qquad (3)$$

Taking $V(r) = \frac{r}{a} V_A$ and assuming D and V_A constant this yields at steady state a Gaussian shape profile for the total impurity density $n_T = n_T(0) \exp(- Sr^2/a_L^2)$ with a peaking parameter $S = a_L V_A/2D$.

Figure 10 shows the profiles of T_e and n_e obtained from ECE and interferometric measurements which have been used for the numerical simulations. The solid lines and the dashed lines represent the profiles measured at the sawtooth's peak and trough, respectively, for the ohmic and RF heated discharges. Intermediate profiles with discontinuous jumps are also used to describe the change in n_e and T_e which occurs during a sawtooth cycle. Numerically, the limiter radius a_L = 1.06 m, the last mesh radius a = 1.10 m, R = 0 and $V_o = 10^3$ m/s. $\tau_{//}$ is set equal to 10 ms in the scrape-off layer and to infinity elsewhere. The crucial choice of Γ_{ext}, on the other hand, requires some discussion.

In laser blow-off impurity injection experiments the simulation of peripheral line brightnesses is a well known difficulty [8]. To illustrate this, Fig.11 shows the Ni XVIII, Ni XXV and Ni XXVI line brightnesses and the soft X-ray signal, measured during such an injection experiment, as a function of time. These data are typical of most injection experiments in JET. Simulations have indicated that the simulated low ionisation potential ion lines like Ni XVIII follow relatively closely the shape of the source function $\Gamma_o(t)$. Therefore these lines cannot be reproduced correctly when an instantaneous atoms burst is used for $\Gamma_o(t)$. This could be explained by an initial recycling of the impurities which is assumed negligible in the simulation or by a modification of the transport parameters near the plasma periphery which are assumed constant in the simulation. To avoid the consideration of such unknown plasma boundary effects and neverthless take them properly into account, it is possible to use instead a source function which has roughly the same shape as the peripheral lines as done in Ref.[6]. In the present work $\Gamma_o(t)$ is represented by a triangular pulse of amplitude Γ_{MAX} with increasing and decreasing times of T_1 and T_2 respectively, followed by a weak exponential tail with time constant τ_L starting at T_3 when $\Gamma_o = \alpha\Gamma_{MAX}$ in the

decreasing part of the pulse. Both the peripheral lines and the X-ray data point out to the necessity for such a source function prolonged by an exponential tail.

The simulation of the soft X-ray data is made taking into account the filter transmission and calculating both the continuum spectrum, due to free-free and free-bound transitions, and the line radiation. In the case of Ni these include the K_α lines around 7.8 keV due to He-like and H-like ions and the associated satellites from B to He-like ionisation stages and in the case of Mo the L-line spectrum between 2.6 and 3.3 keV from Ne-like to Li-like ions. A detailed account of the data subroutines which have been used to evaluate the rate coefficients needed to solve the transport equations (1) and to calculate the line brightnesses and soft X-ray emissivities is given in Ref.[23].

4. IMPURITY TRANSPORT SIMULATIONS

The impurity transport parameters D and V have been determined by simulating the evolving soft X-ray emissivity profiles during the quiescent phase of the sawtooth. When many sawteeth needed to be considered such as in the Ni injection experiment the impurity distribution after each sawtooth crash was used as a new initial condition. The final transport parameters given are those which provide the best overall agreement. In practice, for the numerical simulation, the effect of each sawtooth on the impurity density distribution was described using modified transport parameters over a period of time of the order of the sawtooth crash phase. Discontinuous jumps for the T_e and n_e profiles were included in the simulation to account for the changes these parameters suffer during a sawtooth cycle. In Section 4.1 the simulation of the Mo and Ni injection experiments are discussed and the transport parameters derived during the quiescent phase of the sawteeth are given. The heuristic approach which has been used to describe impurity transport during the sawtooth crash is described in Section 4.2.

4.1 Derivation of D and V

As suggested by the experimental observations it has been assumed that the plasma transport properties can be described considering two regions with distinct transport properties and a transition region between. In each region the diffusion coefficient D and the scaling factor V_A for the

convection velocity $V = \frac{r}{a} V_A$ are assumed constant with radius. The extent of the central region and the value of the diffusion coefficient in each region is obtained by simulating the evolution of the X-ray profile during the inflow phase. During this phase, transport is dominated by diffusion because the impurity density gradient is large and therefore the calculation is not very sensitive to the convection velocity. On the other hand, during the outflow the decay of the emissivity profile is sensitive to the ratio V_A/D allowing V_A to be better determined. The final values for D and V_A are obtained by iteration finding the combination which best reproduces the inflow and outflow phase.

The values of D and V which best reproduce the evolution of the X-ray profile following Mo injection into an RF heated discharge and Ni injection into an ohmically heated discharge are shown in Fig.12. In both cases reduced values are needed for the transport coefficients D and V in the central region. Clearly the error bars shown on the figure can accommodate a radial dependence for D and V_A which for simplicity have been assumed constant with radius for $r < 0.25$ m and $r > 0.4$ m and connected smoothly between 0.25 and 0.4 m. For $r > 0.4$ m the D and V_A values during RF are larger than the ohmic values by a factor 3 and equal to 3 m^2/s and 6 m/s, respectively; in the ohmic case they are 1 m^2/s and 2 m/s. In the central region compared to the outside region the D and V_A ohmic values are reduced by a factor 30 and 20 to 0.03 m^2/s and 0.1 m/s, respectively, and the D and V_A values during RF are reduced by a factor 20 and 10 to 0.15 m^2/s and 0.6 m/s respectively.

Simulation results for the central chord brightness can be seen in Fig.3 and Fig.7 for the ohmic and RF heated cases respectively. A comparison between the measured and calculated X-ray profiles at selected times is shown in Fig.13 for the ohmic case and in Fig.14 for the RF heated case. In these two figures the effect of varying the central value of the diffusion coefficient is also shown. Transport is more easily studied during the RF heated discharge because of the long period of the sawtooth. Figure 15 shows for this case a comparison between the measured and calculated X-ray emissivity as a function of time at two specific radii (r=0 and r=0.35m where the emissivity is maximum during the inflow) and the sensitivity of the simulations to various values of V_A and D. The simulations are performed using a source function defined by: $\Gamma_{MAX} = 6.5\times10^{18}$ atoms/m^2s (for $D = 3$ m^2/s), $T_1 = 15$ ms, $T_2 = 30$ ms, $\alpha = 0.3$ and $\tau = 60$ ms. It reproduces the shape of the peripheral lines and their long decay time reasonably well.

τ = 60 ms is also needed to reproduce the flat maximum of the emissivity at 0.35 m. This illustrates how the transport coefficients shown in Fig.12 have been derived. A similar procedure was followed to derive the transport parameters in the ohmic case.

4.2 Simulation of the Impurity Behaviour During the Sawtooth Crash

The soft X-ray emissivity profiles in Figs. 5 and 8 show clearly a "discontinuity" of the impurity transport at the sawtooth crashes which cannot be simulated by considering the T_e drop alone. At each crash impurity transport is greatly enhanced over the central region leading to a major redistribution of the impurity density. Following the ideas developed in Ref.[12] the ion distribution modification at the sawtooth crash has been described heuristically by increasing both D and V_A by orders of magnitude during a crash period lasting 100-200 μs. Figure 16 shows (solid lines) the D and V_A curves which best reproduce the emissivity profile modification for the monster sawtooth crash during Mo injection. Figure 17 shows on the left the simulated (dashed line) and experimental (solid line) emissivity profiles after the crash. The emissivity profile before the crash is shown in Fig.14. The dot-dashed line of Fig.17 is obtained by using the dashed curve for D given in Fig.16 and no "perturbation" for V_A. This simulation implies a flattening of the Mo ion total density profile $n_T(r)$ up to a mixing radius 30% larger than the sawtooth inversion radius. It is clear from the difference between the dashed and dot-dashed curves of Fig.17 (left) that more Mo has to be pushed towards the plasma centre and this has been obtained by increasing V_A at and just outside the sawtooth inversion radius, with simultaneous limitation of the radial extension of the flat D region. The difference between the two simulations appears clearly in Fig.17 (right), where the simulated $n_T(r)$ is shown just before the crash (dotted line) and at the end of the crash simulation (dashed line for both D- and V_A-perturbations, dot-dashed line for only D-perturbation).

Using similar D and V_A perturbed profiles it is possible to simulate the two inverted sawteeth shown in Fig.5 for the Ni injection experiment. During the outflow perturbed diffusion coefficients similar to the dashed curve in Fig.16 need to be used for the sawtooth crashes. However, different adjustments of the perturbation amplitude and duration are necessary to simulate the individual sawteeth.

In conclusion the abrupt change in impurity transport which occurs during a sawtooth crash has been described heuristically by increasing the transport parameters used during the quiescent phases by several orders of magnitude. However, a unified description has not been found since ad hoc adjustments of the transport perturbation have been proved to be necessary for each sawtooth. This is probably due to the fact that the adopted description, which is based on a one dimensional model implies a unidirectional flow of impurities at every radial position; in reality the observed phenomena point to exchange of matter at the crash in both directions across the q=1 surface. Moreover, the complex phenomena are not poloidally symmetric, as evidenced by the complex structures observed at the crashes, implying poloidally asymmetric movements of hot and cold zones across the q=1 surfaces [21].

5.1 SUMMARY AND CONCLUSION

Small quantities of high-Z impurities have been injected into JET plasmas by laser blow-off to study impurity transport. The progression of the impurities into the plasma was followed with good spatial and temporal resolution using two soft X-ray cameras and was simulated using an impurity transport code yielding values for the radially dependent transport coefficients D and V. Two discharge regimes, ohmic and RF heated plasmas, have been compared by focussing on the detailed analysis of two representative discharges.

The results clearly show, for both cases, that impurity transport is much smaller in the central region of the plasma than outside of it and greatly enhanced during sawtooth crashes. The values of the transport coefficients which best reproduce the experimental data in the transport simulation are given in Fig.12 and summarised below.

OH plasma (D_2, #17661)

(I_p=3MA, B_t=3.2T, n_{eo}=2×10^{19}m^{-3}, T_{eo}=4000eV, Z_{eff}=5)

D_A = 0.03 m^2/s V_A = 0.1m/s	for r < 0.25 m	
D_A = 1 m^2/s V_A = 2 m/s	for r > 0.4 m	

RF heated plasma (D_2, #18112)

(I_p=3MA, B_t=3.2T, n_{eo}=2.9×10^{19}m^{-3}, T_{eo}=9000eV, P_{RF}=6MW, Z_{eff}=3)

D_A = 0.15 m^2/s V_A = 0.6 m/s	for r < 0.25 m	
D_A = 3 m^2/s V_A = 6 m/s	for r > 0.4 m	

These values can be compared with the predictions of the neoclassical theory and electron transport measurements available on JET. For the neoclassical calculations it has been assumed that $T_i = T_e$ and only collisions with the deuterium ions were considered taking Ni^{+26} and Mo^{+38} as representative ions for the ohmic and RF case respectively. The measured values of the diffusion coefficient are a factor 2 and 5 higher than the neoclassical values for the central region and a factor 300 and 60 higher at 3/4 radius. Thus the measured values are of the same order as the neoclassical values in the central region, agreeing within the error bars in the ohmic case, and "strongly anomalous" outside the central region. Measurements of electron transport on JET using different perturbation methods yield a value of 0.4 m^2/s for D_e and ~ 0.1 m/s for the convection velocity for 3 MA ohmic plasmas in the region between $r/a_L = 0.5$ and $r/a_L = 0.7$ [1]. These are roughly a factor 2 and 10 lower than the corresponding values of D and V measured for the impurities.

A strong reduction of the diffusion coefficient in the central region is probably a general feature of most tokamaks limiter discharges. This then would explain the very peaked and long lasting n_e and soft X-ray profiles following the injection of pellets in the plasma centre which have been observed on different machines [24-27]. Also in the presence of additional heating the peaked profiles decay faster [2]. This is consistent with the observation that the diffusion coefficient is larger in the RF heated case.

A possible explanation for the reduction of the transport parameters in the central plasma region can be found in Ref.[28]. In the model proposed there the magnetic topology in a given plasma region is linked with the shear dq/dr which influences the size and distance between magnetic islands. Outside the q=1 region where $\frac{dq}{dr} > 0$ and $q > 1$ adjacent magnetic islands may overlap causing the magnetic topology to become partially chaotic. The flow of impurities along the chaotic field lines would be responsible for the large value of the diffusion coefficient observed in that region. On the other hand, in the central region the shear is small and the distance between islands is large; the well nested magnetic surfaces are possibly difficult for the impurity to cross explaining the low value of the central diffusion coefficient.

ACKNOWLEDGEMENTS

Special thanks are due to B Denne and M Watkins. We wish to acknowledge also all our colleagues in the JET team who have made this work possible.

REFERENCES

[1] CHEETHAM A D, GONDHALEKAR A, DE HAAS J C M, JARVIS O N, MORGAN P D et al., in Plasma Physics and Controlled Nuclear Fusion Research (Proc. 12th Int. Conf. Nice, 1988) Vol.1, IAEA, Vienna (1989) 483.

[2] JET TEAM (presented by G L Schmidt) ibid., Vol.1, 215.

[3] BEHRINGER K, BOILEAU A, BOMBARDA F, DENNE B, ENGELHARDT W et al., in Plasma Physics and Controlled Nuclear Fusion Research (Proc. 11th Int. Conf. Kyoto, 1986) Vol.1, IAEA, Vienna (1987) 197.

[4] HAWKES N, WANG Z, BARNSLEY R, BEHRINGER K, COHEN S et al., in Controlled Fusion and Plasma Physics (Proc. 16th Eur. Conf. Venice, 1989) Vol.13B, Part I, European Physical Society (1989) 79.

[5] MARMAR E S, RICE J E, TERRY J L and SEGUIN F H, Nucl.Fusion 22(1982) 1567.

[6] TFR GROUP, Nucl.Fusion 25(1985) 1767.

[7] SUCKEWER S, CAVALLO A, COHEN S, DAUGHNEY C, DENNE B et al., Nucl.Fusion 24(1984) 815.

[8] STRATTON B C, FONCK R J, HULSE R A, RAMSEY A T, TIMBERLAKE J et al., Nucl.Fusion 29(1989) 437.

[9] ROTH J and JANESCHITZ G, Nucl.Fusion 29(1989) 915.

[10] PETRASSO R, SEGUIN F H, LOTER N G, MARMAR E and RICE J, Phys.Rev.Lett. 49(1982) 1826.

[11] SEGUIN F H, PETRASSO R and MARMAR E S, Phys.Rev.Lett. 51(1983) 455.

[12] COMPANT LA FONTAINE A, DUBOIS M A, PECQUET A L, BOYD D, CAVALLO A, COHEN S et al., Plasma Phys.Contr.Fusion 27(1985) 229.

[13] CAMPBELL D J, GILL R D, GOWERS C W, WESSON J A, BARTLETT D V et al., Nucl.Fusion 26(1986) 1085.

[14] CAMPBELL D J, START D F H, WESSON J A, BARTLETT D V, BHATNAGAR V P et al., Phys.Rev.Lett. 60(1988) 2148.

[15] MAGYAR G, BARNES M R, COHEN S, EDWARDS A W, HAWKES N C, PASINI D and ROBERTS P J, JET Report JET-R(88)15.

[16] EDWARDS A W, FAHRBACH H U, GILL R D, GRANETZ R, OORD E, SCHRAMM G, TSUJI S and ZASCHE D, Rev.Sci.Instrum. 57(1986) 2142.

[17] GRANETZ R S and SMEULDERS P, Nucl.Fusion 28(1988) 457.

[18] PASINI D, GILL R D, HOLM J, VAN DER GOOT E and WELLER A, Rev.Sci Instrum. 59(1988) 693.

[19] BRAITHWAITE G, GOTTARDI N, MAGYAR G, O'ROURKE J, RYAN D and VERON D, Rev.Sci.Instrum. 60(1989) 2825.

[20] BARTLETT D V, BAKER E A M, CAMPBELL D J, and COSTLEY A E, Rev.Sci.Instrum. 56(1985) 940.

[21] EDWARDS A W, CAMPBELL D J, ENGELHARDT W, FAHRBACH H U, GILL R D et al., Phys.Rev.Lett. 57(1986) 210.

[22] TFR GROUP, Nucl.Fusion 25(1985) 981.

[23] PASINI D, MATTIOLI M, EDWARDS A W, GIANNELLA R, GILL R D et al., JET Report JET-P(90)01.

[24] PETRASSO R D, SIGMAR D J, WENZEL K W, HOPF J E, GREENWALD M et al., Phys.Rev.Lett. 57(1986) 707.

[25] HULSE R A, EFTHIMION P, GREK B, HILL K, JOHNSON D et al., in Controlled Fusion and Plasma Physics (Proc. 14th Eur. Conf. Madrid, 1987) Vol.11D, Part I, European Physical Society (1987) 318.

[26] BEHRINGER K, DENNE B, GOTTARDI N, VON HELLERMANN M and PASINI D, Presented at the IAEA Commission Meeting on Pellet Injection and Toroidal Confinement, Gut Ising, FRG, 1988.

[27] PASINI D, EDWARDS A, GILL R, WELLER A and ZASCHE D, in Controlled Fusion and Plasma Heating (Proc. 15th Eur. Conf. Dubrovnik, 1988) Vol.12B, Part I, European Physical Society (1989) 251.

[28] REBUT P H and BRUSATI M, Plasma Physics and Contr.Fusion 28(1986) 113.

A P P E N D I C E S

1. ATOMIC DATA FOR NICKEL

Recommended data on atomic collision processes involving Fe and its ions have been published in the Nuclear Fusion Special Supplement 1987. The suggested ionisation rates for Fe ions have been introduced in our code, including the recently discovered error for highly charged ions starting from the Ne-like sequence [A1]. For all these ions the recommended rates and cross-sections have to be multiplied by a factor of 1.629.

For Ni ions assessed data are available for a few ions (Ni I-IV [A2], Ni VI-IX [A3] and Ni XVIII [A4]), for the remaining ions some "scaling" from the recommended Fe data is necessary. For direct ionisation the same four Younger's parameters can be taken for Ni as for Fe. Inner-shell excitation followed by autoionisation (ISEA) has to be added for most of the ions up to the Na-like sequence. Since its contribution cannot be scaled directly from the Fe data, for Ni XIII-XVII (S-like to Mg-like ions) we use the prescriptions of Ref.[A5]. For the remaining ions only rough evaluation is possible, supposing ISEA to contribute similarly for both Fe and Ni ions of the same sequence. This implies multiplication of the direct ionisation rates by a factor of one for Ni V and by a factor of two for Ni X-XII.

The recombination rate coefficients α_Z^R are obtained as described in [A6], while the charge-exchange recombination rate coefficients α_Z^{CX} are evaluated using the scaled reduced cross-sections proposed in [A7]. It is supposed that both the recombining ions and the D^+ ions have the same temperature T_i as the neutral deuterium atoms T_D and that this temperature can be taken equal to T_e, at least in the external plasma region. Note that deuterium is the JET filling gas.

Line brightnesses and emissivities are predicted for the strong $\Delta n=0$ ns-np transitions of the Mg-like, Na-like, Be-like and Li-like sequences in the coronal population approximation. The needed excitation rate coefficients have been taken in [A8].

The radiations detected by the soft X-ray diodes are simulated taking into account both the continuum spectrum due to free-free and free-bound transitions and the line radiation of the so-called K_α spectrum, including the He-like and H-like 1s-2p lines and the associated satellites with line upper levels populated either by dielectronic recombination or by inner-shell excitation. The free-bound spectrum is calculated [A9] using usual formulae for radiative recombination to form H-like ions, modified to take into account that the valence shell can be partially filled and that its ionisation potential is not hydrogen-like. Excited levels are considered hydrogen-like. For both bremsstrahlung and radiative recombination the Gaunt factors are taken equal to unity. Attenuation of the 250μm Be filter has been taken into account roughly by the introduction of a cut-off energy at 2.5 keV. Similarly the diode transparency threshold towards high photon energies is assumed to be at 25 keV. For more detailed calculations the so-called X-ray spectral efficiency of the assembly filter plus detector should be evaluated as function of the photon energy.

The K_α spectrum is evaluated in the following way: the He-like w and H-like Lyman α lines are taken from [A8] where analytical formulae are given (for the w line there is good agreement with [A10]), the He-like triplet (x+y+z) to singlet (w) ratio is taken from [A10], as well as the intensity of the He-like, Li-like, Be-like and B-like satellites (we have added the contribution of all the 1s-2p lines included in [A10], considering the contributions of both dielectronic recombination and inner-shell excitation). Finally the H-like ion recombination contribution to the x, y, z and w lines is included following [A10].

2. ATOMIC DATA FOR MOLYBDENUM

Ionisation equilibrium and radiative losses were in the past evaluated for Mo [A9] to analyse quantitatively the old TFR experimental results. Since available atomic data for Mo are not as developed as for lighter elements up to Ni, one has to rely only on general formulae. Consequently we have only updated the old calculations.

The ionisation rate coefficients S_Z have been evaluated as in [A9] using the Lotz's formula, but inner-shell excitation followed by autoionisation has been introduced for P-like to Na-like ions according to the prescriptions of

Ref.[A11]. For dielectronic recombination the well known Merts' modification for $\Delta n=1$ transitions has been added to the original Burgess' formula. Charge exchange recombination is available using the scaled reduced cross-sections proposed in [A7].

The continuum radiation has been estimated as for Ni with the same cut-off energy of 2.5 keV towards low photon energies. The L-line spectrum (between 2.6 and 3.3 keV) is due to 2-3 transitions of Ne-like to Li-like ions. It has been evaluated using the well known so-called Van Regemorter-Mewe formula for $\Delta n=1$ transitions for each of the indicated ions. The global excitation rate Q (cm^3/s) is given by

$$Q = \frac{1.6\ 10^{-5}\ f\ g\ (\beta)\ \sqrt{\beta}}{\Delta E^{\ 3/_2}} \qquad (A.1)$$

$\beta = T_e/\Delta E$, ΔE in eV is the average excitation energy of the involved transitions, $g(\beta) = 0.15 + 0.28\ e^{\beta}\ E_1(\beta)$ (E_1 indicating the exponential integral function), f is the absorption oscillator strength. For F-like, O-like, N-like ions the following values were taken 3.5, 2.1 and 1.35. For F-like ions the values of 5.0 (used in [A9]) has been reduced since giving too large values for the Fe and Ni dielectronic recombination rate coefficients [A6], for O-like and N-like ions the values of [A12,A13] were extrapolated up to Mo. For Ne-like, C-like, B-like and Be-like ions Bhatia et al. [A14-A17] have calculated oscillator strengths, radiative decay rates, electron collision strengths and line intensities up to Kr ions for a single electron temperature equal to half the ionisation potential. We calculated for each sequence and each element an equivalent excitation rate coefficient for all the 2-3 transitions included in Bhatia's papers. These values were extrapolated to Mo and allowed determination of f using formula (A.1). We obtained, respectively, for Ne-, C-, B- and Be- like ions 4.75, 1.85, 0.8, 1.2. For Li-like ions the calculations of [A18] (essentially formula (A.1) with $g(\beta)$ slightly modified) were used for the 3 strong lines 2s-3p, 2p-3d and 2p-3s. Since all these L-lines have photon energies increasing from ~2.6 keV (for Ne-like ions) up to ~3.3 keV (for Li-like ions) transmission of the 250μm thick Be filter has been considered for each ionisation stage [A19].

The procedure followed to evaluate Mo L-line intensities has been applied also to include in the code Fe and Ni L-line intensities, with the advantage

that Bhatia's calculations can be used directly for these two elements. In the case of JET these lines are below the absorbing filter cut-off energy.

REFERENCES

[A1] PINDZOLA M S, GRIFFIN D C, BOTTCHER C, YOUNGER S M and HUNTER H T, Nuclear Fusion Special Supplement 1987, 21.

[A2] LENNON M A, BELL K L, GILBODY H B, HUGHES J G, KINGSTON A E et al., J.Phys.Chem.Ref.Data 17(1988) 1285.

[A3] WANG L J, RYNN K and GREGORY D C, J.Phys.B 21(1988) 2117.

[A4] GRIFFIN D C, PINDZOLA M S and BOTTCHER C, Phys.Rev.A 36(1987) 3642.

[A5] ARNAUD M and ROTHENFLUG R, Astron.Astrophys.Suppl.Ser. 60(1985) 425.

[A6] MATTIOLI M, Cadarache Laboratory Report EUR-CEA-FC 1346(1988).

[A7] PHANEUF R A, JANEV R K and HUNTER H T, Nucl. Fusion Special Supplement 1987, 7.

[A8] CLARK R E H, MAGEE N H, MANN J B Jr and MERTS A L, Astrophys.J. 254(1982) 412.

[A9] BRETON C, DE MICHELIS C and MATTIOLI M, J.Quant.Spectrosc.Radiat. Transfer 19(1978) 367.

[A10] BOMBARDA F, GIANNELLA R, KÄLLNE E, TALLENTS G J, BELY-DUBAU F et al., Phys.Rev.A 37(1988) 504.

[A11] BURGESS A and CHIDICHIMO M C, Mon.Not.R.Astr.Soc. 203(1983) 1269.

[A12] FAWCETT B C, Atomic Data Nuclear Data Tables 34(1986) 215.

[A13] BROMAGE G E and FAWCETT B C, Mon.Not.R.Astr.Soc. 179(1977) 683.

[A14] BHATIA A K , FELDMAN U and SEELY J F, Atomic Data Nuclear Data Tables 32(1985) 435.

[A15] BHATIA A K, SEELY J F and FELDMAN U, Atomic Data Nuclear Data Tables 36(1987) 453.

[A16] BHATIA A K, FELDMAN U and SEELY J F, Atomic Data Nuclear Data Tables 35(1986) 319.

[A17] BHATIA A K, FELDMAN U and SEELY J F, Atomic Data Nuclear Data Tables 35(1986) 449.

[A18] COCHRANE D M and McWHIRTER R W P, Physica Scripta 28(1983) 25.

[A19] WELLER A, PASINI D, EDWARDS A W, GILL R D and GRANETZ R, JET Report JET-IR(87)10.

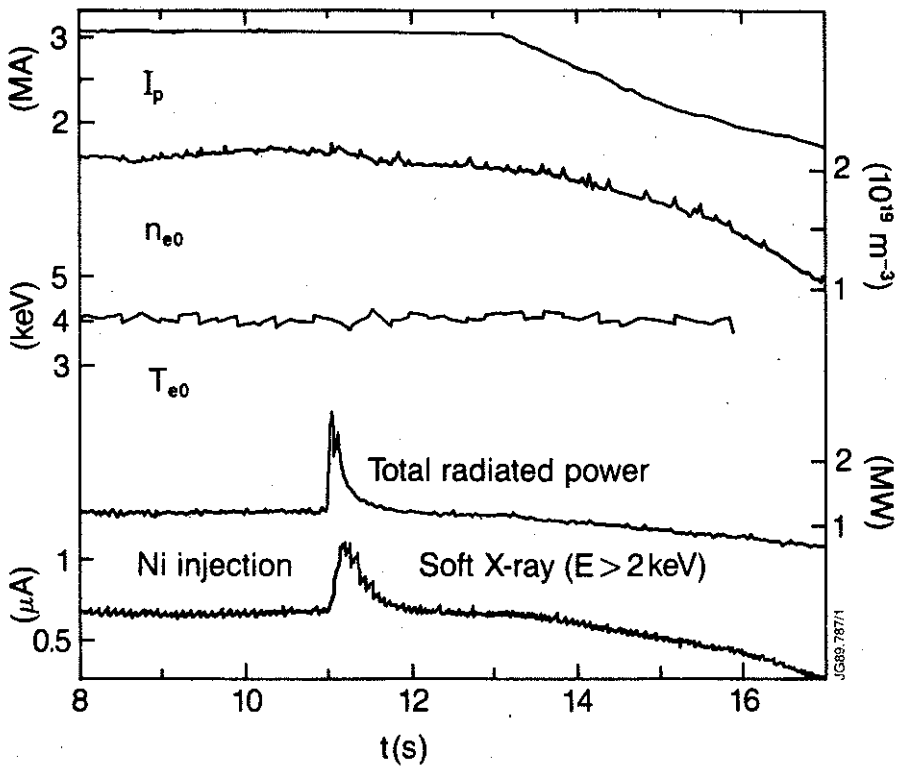

Fig. 1Time evolution of the plasma current I_p, central electron density n_{eo}, central electron temperature T_{eo}, total radiated power and soft X-ray signal. Ni is injected into the discharge at 10.990s (plasma pulse # 17661).

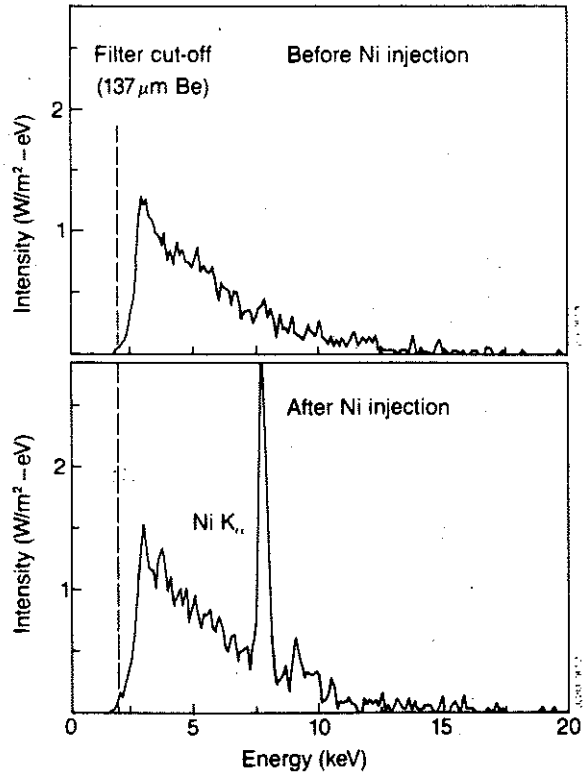

Fig. 2 PHA spectra before and after Ni injection for the same plasma pulse as Fig. 1.

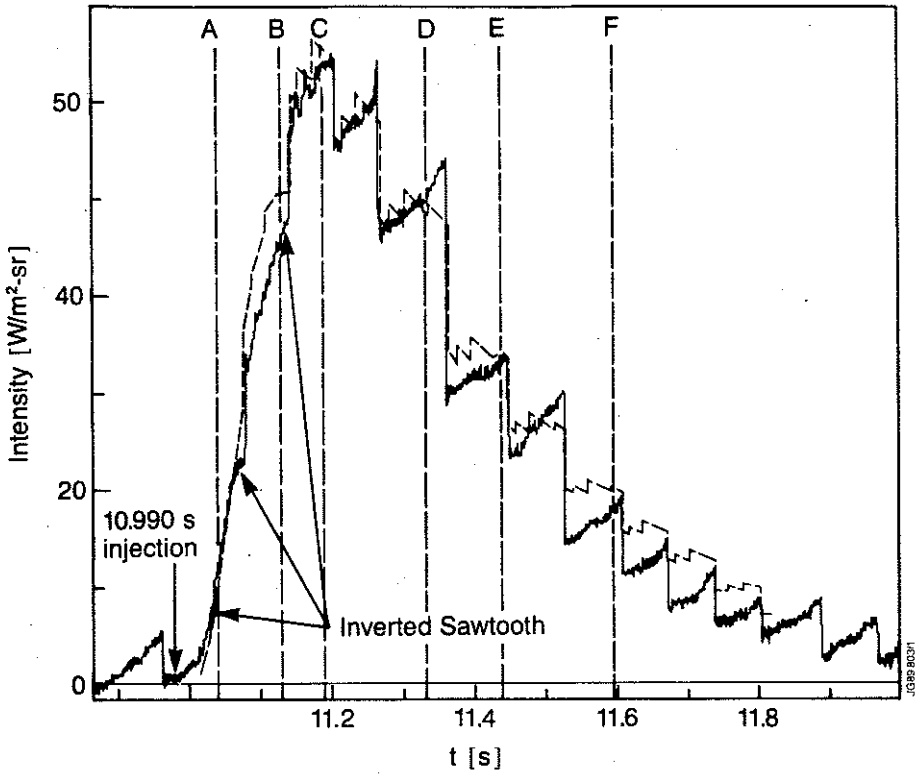

Fig. 3 Central chord soft X-ray signal around the time of Ni injection with the background emission subtracted. The dashed line represents the results of a simulation discussed in Section 4.1. The vertical dashed lines A to F show the times for the tomographic reconstructions shown in Fig. 4.

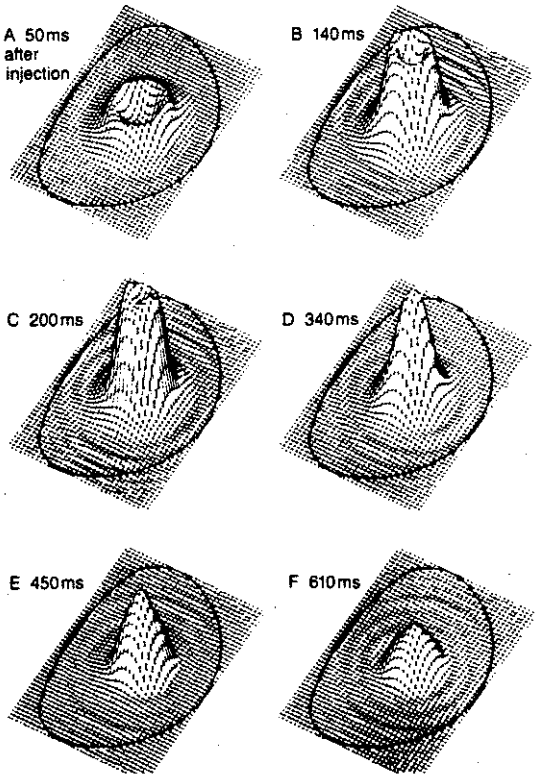

Fig. 4 Evolution of the X-ray emissivity distribution (background emission subtracted) following Ni injection as reconstructed from the line integrated measurements for the times indicated and corresponding to the dashed lines in Fig. 3.

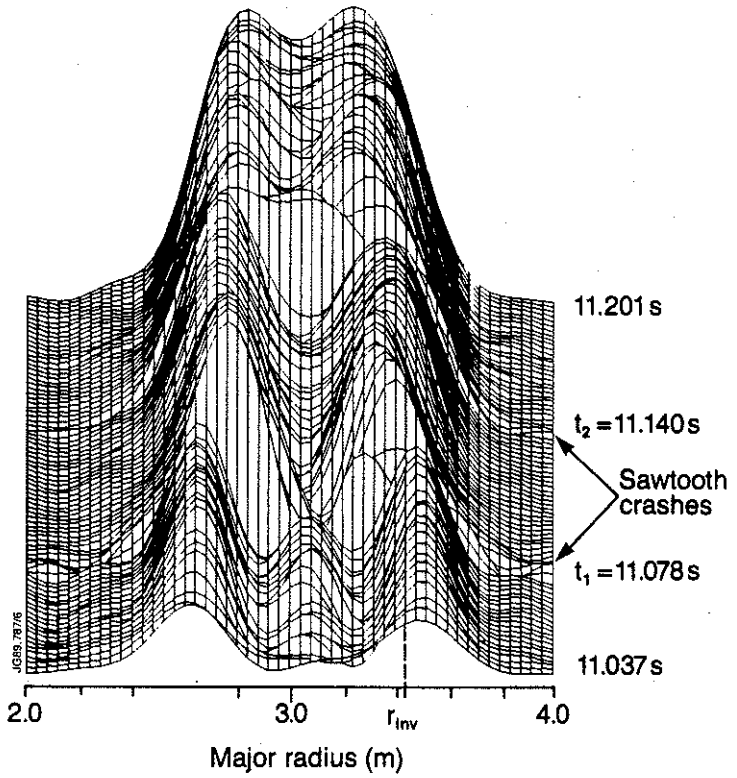

Fig. 5 Evolution of the X-ray emissivity distribution along a horizontal central chord starting 47 ms after blow-off and ending 163 ms later, just before the maximum of the X-ray signal. The dashed line shows the sawtooth inversion radius obtained from tomography. There is a sawtooth crash at $t_1 = 11.078$ s and $t_2 = 11.140$ s.

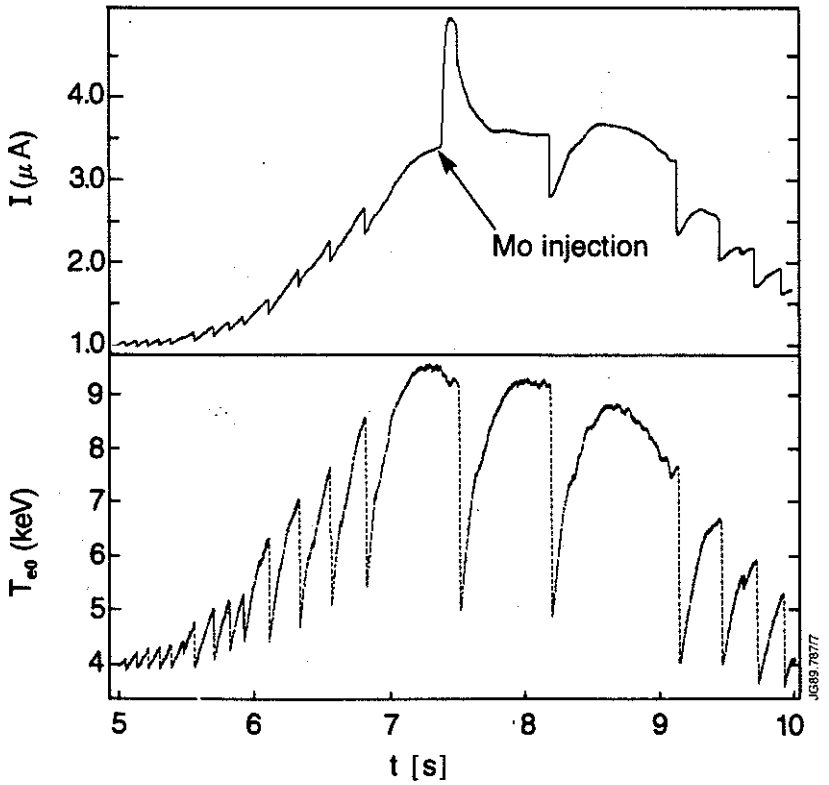

Fig. 6 Central chord soft X-ray signal and central electron temperature for a 3 MA discharge additionally heated with 6 MW of RF power. Mo is injected at 7.387 s, 133 ms before the monster sawtooth crash at 7.520 s (plasma pulse # 18112).

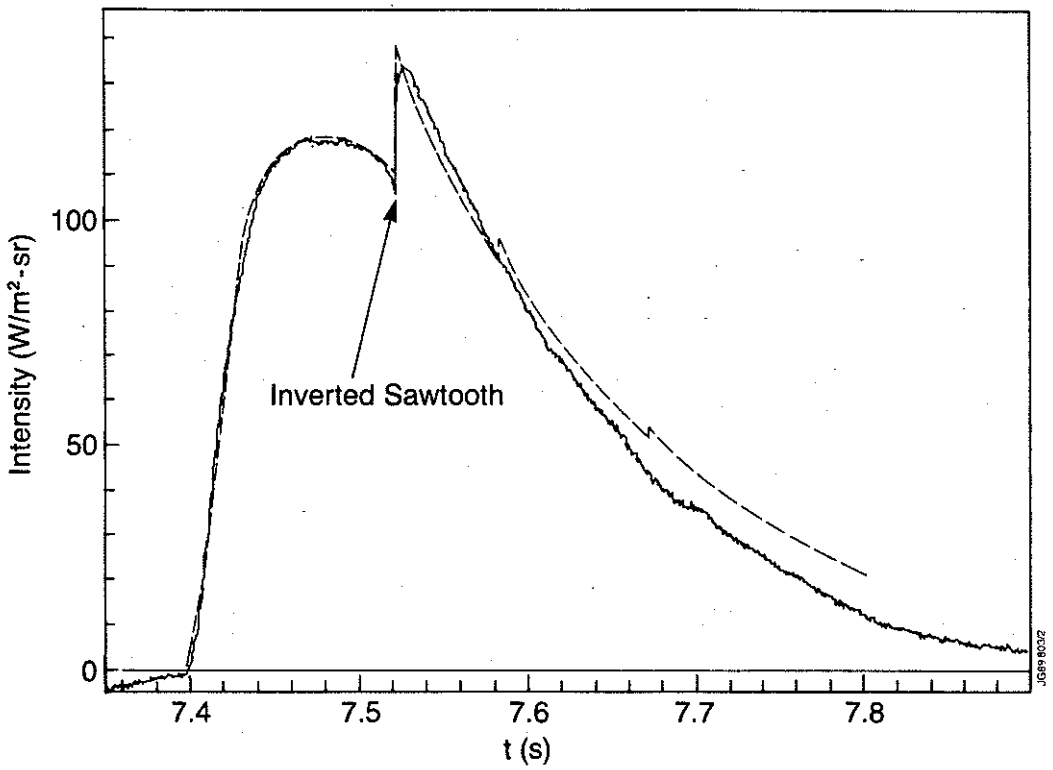

Fig. 7 Central chord soft X-ray signal around the time of Mo injection with the background emission subtracted. The dashed line represents the results of a simulation discussed in Section 4.1.

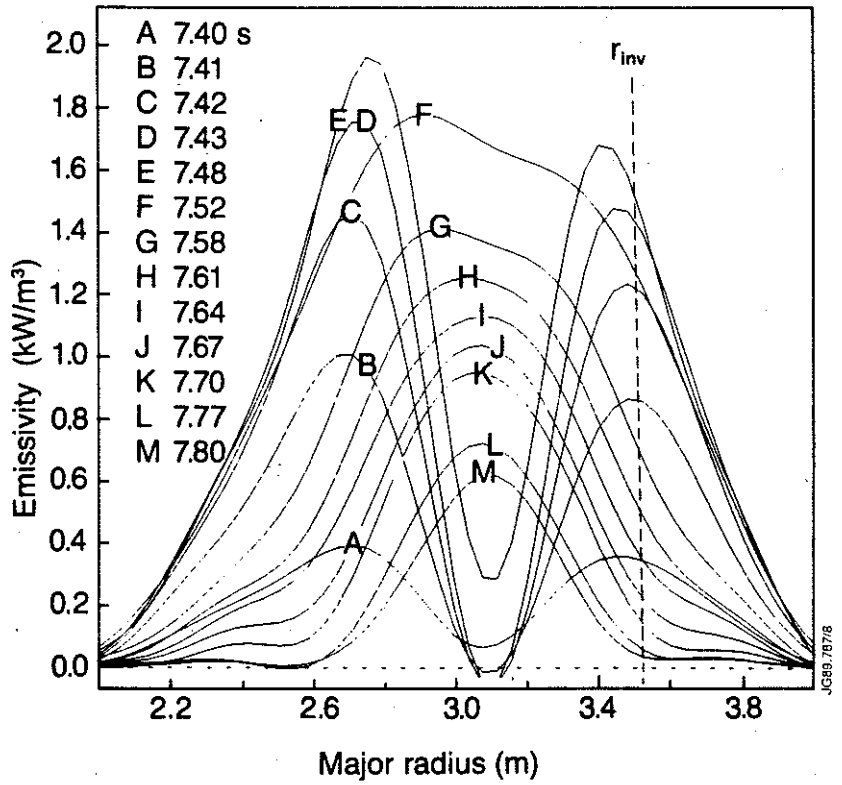

Fig. 8 Evolution of the X-ray emissivity distribution (background emission subtracted) along a horizontal central chord after Mo injection. The dashed line shows the sawtooth inversion radius obtained from tomography. After the sawtooth crash at 7.520 s (curves F-M) the emissivity profiles are peaked in the plasma centre.

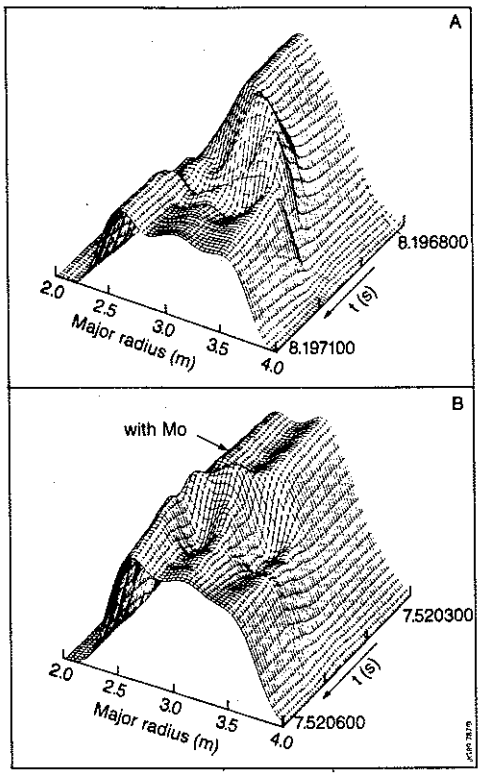

Fig. 9 Time evolution (300 μs total) of the total X-ray emissivity (no background subtraction) along a horizontal central chord during a sawtooth crash (# 18112). Figure (A) is for the sawtooth at 8.197 s free of Mo radiation. Figure (B) is for the sawtooth at 7.520 s and shows the modification of the X-ray emission due to Mo impurities.

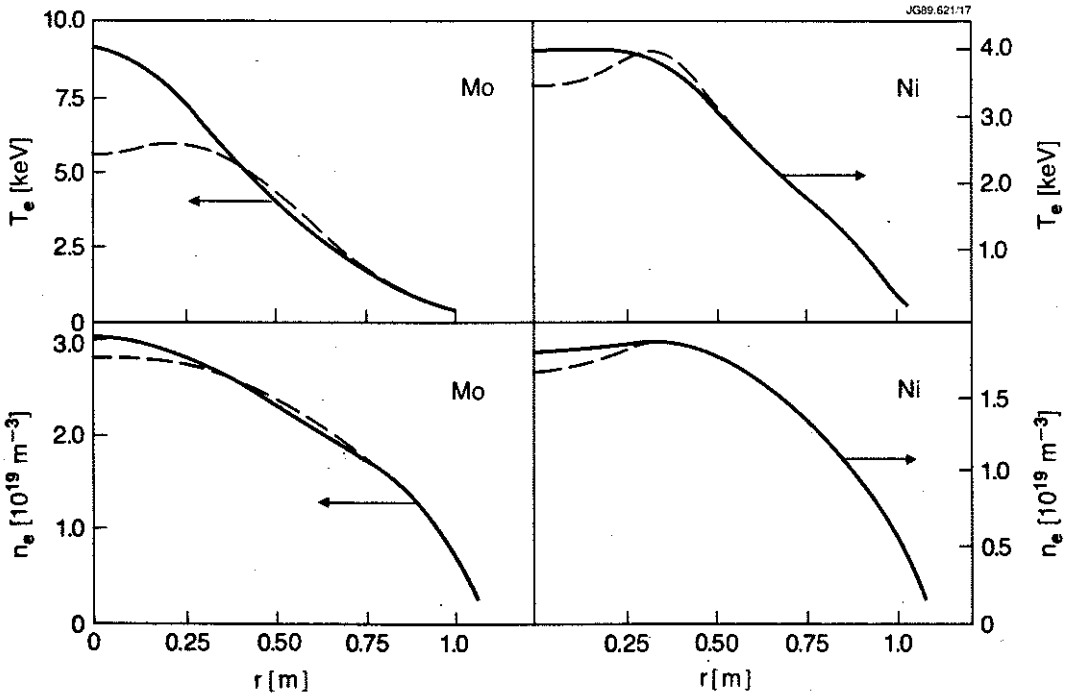

Fig. 10 T_e and n_e radial profiles used for the numerical simulations (left: Mo injection, right: Ni injection). The solid and dashed lines show the profiles at the peak and at the trough of a sawtooth respectively.

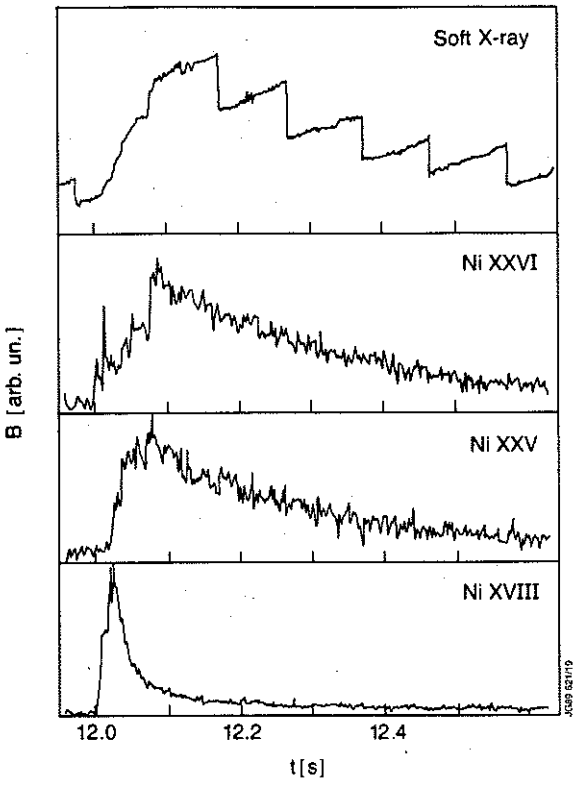

Fig. 11 Reference soft X-ray signal, brightnesses of three VUV lines (Ni XXVI 165Å, Ni XXV 118Å, Ni XVIII 292Å) detected in another laser blow-off Ni injection into an ohmic plasma similar to the one shown in Fig. 1. The lack of delay on the Ni XXVI brightness is due to blended low ionisation potential Ni ion lines.

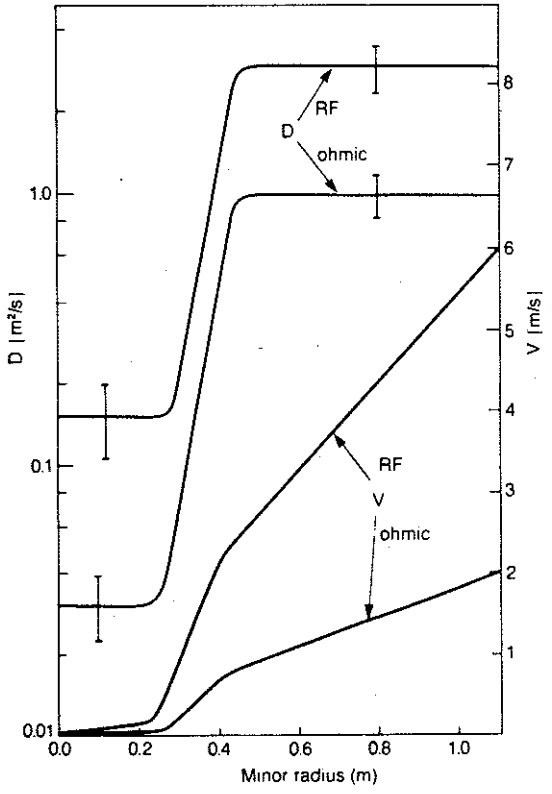

Fig. 12 Radial profile of D (logarithmic scale on the left) and of V (linear scale on the right) used to simulate the injection on Ni into an ohmic plasma and the injection of Mo into an RF heated plasma.

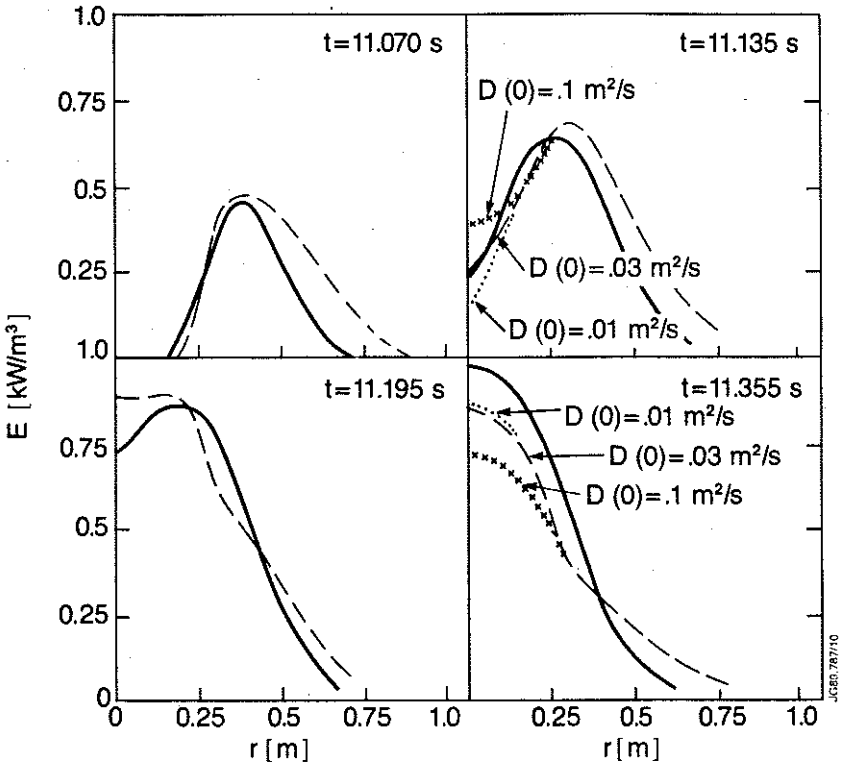

Fig. 13 Experimental (solid line) and simulated (dashed line) profiles, respectively, at t = 11.070 s, 11.135 s, 11.195 s and 11.355 s for Ni injection, using the D and V curves shown in Fig. 12. The effect of varying the central value of the diffusion coefficient is shown for the profiles at t = 11.135 s and t = 11.355 s.

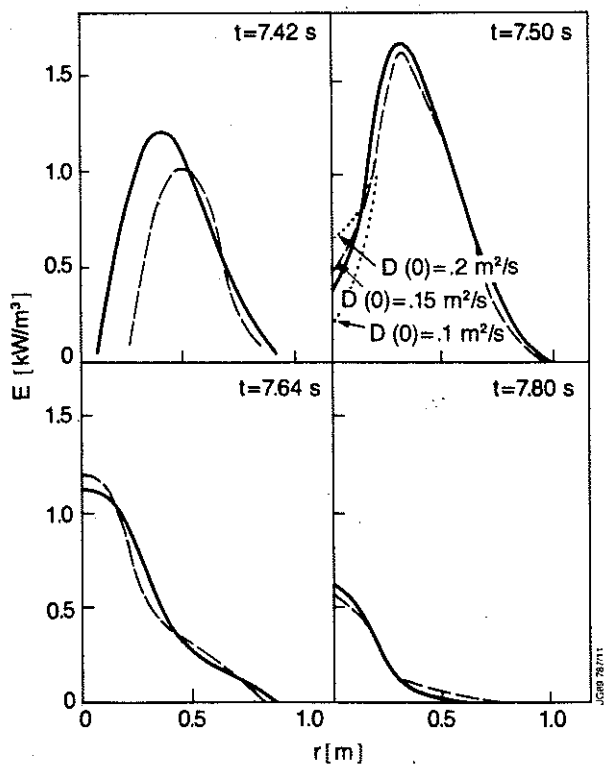

Fig. 14 Experimental (solid line) and simulated (dashed line) profiles, respectively at t = 7.42 s, 7.50 s, 7.64 s and 7.80 s for Mo injection, using the D and V curves shown in Fig. 12. The effect of varying the central value of the diffusion coefficient is shown for the profile at 7.50 s.

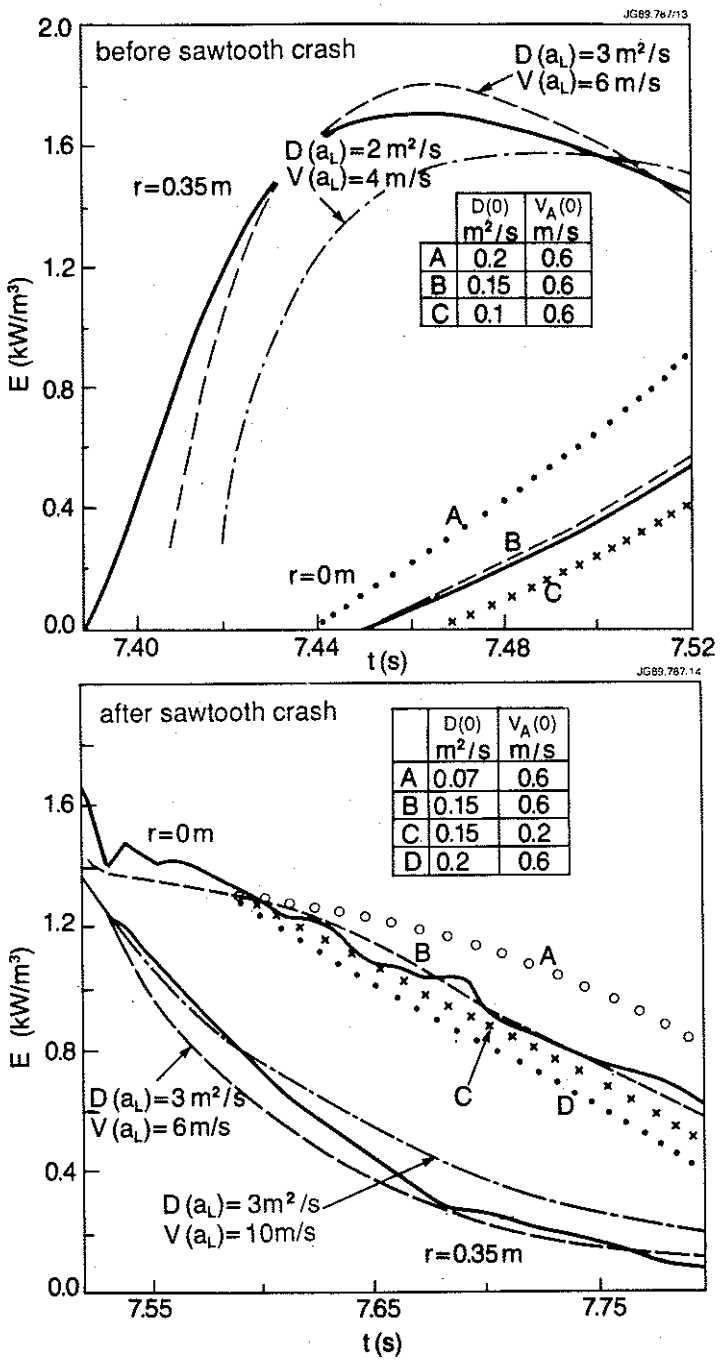

Fig. 15 Comparison between experiment (solid line) and simulation (dashed line) using the D and V curves shown in Fig. 12 for the emissivity as a function of time at two selected radii (r=0 and r=0.35 m). For the simulations at r=0.35 m, $D(0)=0.15\,m^2/s$ and $V_A(0)=0.6\,m/s$. For the simulations at r=0 m, $D(a_L)=3\,m^2/s$, $V(a_L)=6\,m/s$.

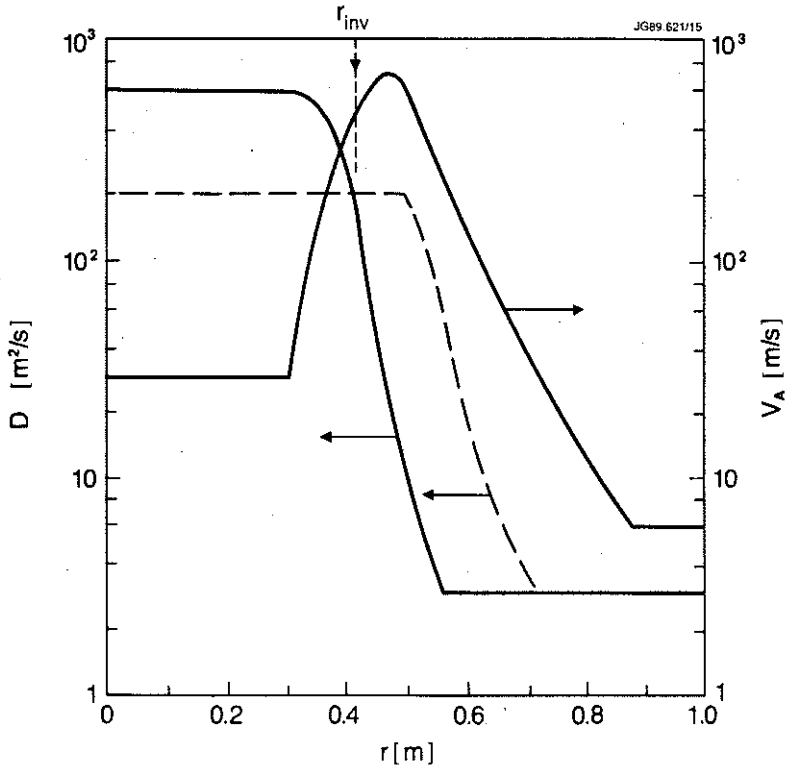

Fig. 16 Solid line: D and V_A curves used to simulate the sawtooth crash at 7.520 s for Mo injection; crash duration $t_c = 200\,\mu s$. Dashed line: D-curve used during the crash to obtain the dot-dashed curves of Fig. 17. The vertical dashed line shows the position of the sawtooth inversion radius.

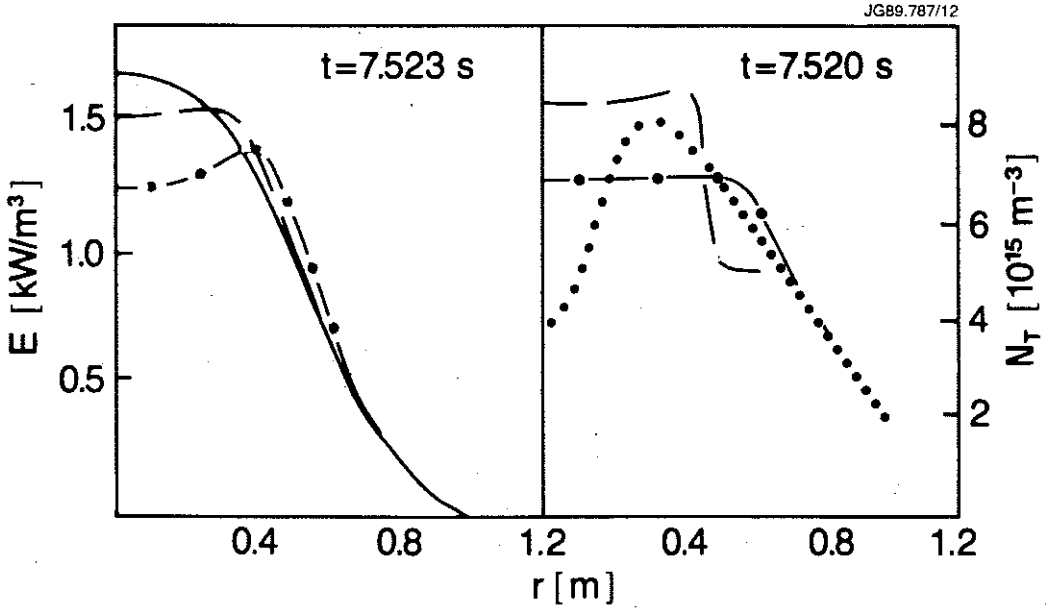

Fig. 17 Left: experimental (solid line) and simulated (dashed line) emissivity profile at 7.523 s i.e. 3 ms after the sawtooth crash. Right: simulated Mo ion total density profiles $n_T(r)$ just before (dotted line) and at the end of the crash lasting $t_c = 200\,\mu s$ (dashed line). Dot-dashed curves: simulation using the dashed curve of D given in Fig. 16.

APPENDIX 1.

THE JET TEAM

JET Joint Undertaking, Abingdon, Oxon, OX14 3EA, U.K.

J.M.Adams[1], F.Alladio[4], H.Altmann, R.J.Anderson, G.Appruzzese, W.Bailey, B.Balet, D.V.Bartlett, L.R.Baylor[24], K.Behringer, A.C.Bell, P.Bertoldi, E.Bertolini, V.Bhatnagar, R.J.Bickerton, A.Boileau[3], T.Bonicelli, S.J.Booth, G.Bosia, M.Botman, D.Boyd[31], H.Brelen, H.Brinkschulte, M.Brusati, T.Budd, M.Bures, T.Businaro[4], H.Buttgereit, D.Cacaut, C.Caldwell-Nichols, D.J.Campbell, P.Card, J.Carwardine, G.Celentano, P.Chabert[27], C.D.Challis, A.Cheetham, J.Christiansen, C.Christodoulopoulos, P.Chuilon, R.Claesen, S.Clement[30], J.P.Coad, P.Colestock[6], S.Conroy[13], M.Cooke, S.Cooper, J.G.Cordey, W.Core, S.Corti, A.E.Costley, G.Cottrell, M.Cox[7], P.Cripwell[13], F.Crisanti[4], D.Cross, H.de Blank[16], J.de Haas[16], L.de Kock, E.Deksnis, G.B.Denne, G.Deschamps, G.Devillars, K.J.Dietz, J.Dobbing, S.E.Dorling, P.G.Doyle, D.F.Düchs, H.Duquenoy, A.Edwards, J.Ehrenberg[14], T.Elevant[12], W.Engelhardt, S.K.Erents[7], L.G.Eriksonn[5], M.Evrard[2], H.Falter, D.Flory, M.Forrest[7], C.Froger, K.Fullard, M.Gadeberg[11], A.Galetsas, R.Galvao[8], A.Gibson, R.D.Gill, A.Gondhalekar, C.Gordon, G.Gorini, C.Gormezano, N.A.Gottardi, C.Gowers, B.J.Green, F.S.Griph, M.Gryzinski[26], R.Haange, G.Hammett[6], W.Han[9], C.J.Hancock, P.J.Harbour, N.C.Hawkes[7], P.Haynes[7], T.Hellsten, J.L.Hemmerich, R.Hemsworth, R.F.Herzog, K.Hirsch[14], J.Hoekzema, W.A.Houlberg[24], J.How, M.Huart, A.Hubbard, T.P.Hughes[32], M.Hugon, M.Huguet, J.Jacquinot, O.N.Jarvis, T.C.Jernigan[24], E.Joffrin, E.M.Jones, L.P.D.F.Jones, T.T.C.Jones, J.Källne, A.Kaye, B.E.Keen, M.Keilhacker, G.J.Kelly, A.Khare[15], S.Knowlton, A.Konstantellos, M.Kovanen[21], P.Kupschus, P.Lallia, J.R.Last, L.Lauro-Taroni, M.Laux[33], K.Lawson[7], E.Lazzaro, M.Lennholm, X.Litaudon, P.Lomas, M.Lorentz-Gottardi[2], C.Lowry, G.Magyar, D.Maisonnier, M.Malacarne, V.Marchese, P.Massmann, L.McCarthy[28], G.McCracken[7], P.Mendonca, P.Meriguet, P.Micozzi[4], S.F.Mills, P.Millward, S.L.Milora[24], A.Moissonnier, P.L.Mondino, D.Moreau[17], P.Morgan, H.Morsi[14], G.Murphy, M.F.Nave, M.Newman, L.Nickesson, P.Nielsen, P.Noll, W.Obert, D.O'Brien, J.O'Rourke, M.G.Pacco-Düchs, M.Pain, S.Papastergiou, D.Pasini[20], M.Paume[27], N.Peacock[7], D.Pearson[13], F.Pegoraro, M.Pick, S.Pitcher[7], J.Plancoulaine, J-P.Poffé, F.Porcelli, R.Prentice, T.Raimondi, J.Ramette[17], J.M.Rax[27], C.Raymond, P-H.Rebut, J.Removille, F.Rimini, D.Robinson[7], A.Rolfe, R.T.Ross, L.Rossi, G.Rupprecht[14], R.Rushton, P.Rutter, H.C.Sack, G.Sadler, N.Salmon[13], H.Salzmann[14], A.Santagiustina, D.Schissel[25], P.H.Schild, M.Schmid, G.Schmidt[6], R.L.Shaw, A.Sibley, R.Simonini, J.Sips[16], P.Smeulders, J.Snipes, S.Sommers, L.Sonnerup, K.Sonnenberg, M.Stamp, P.Stangeby[19], D.Start, C.A.Steed, D.Stork, P.E.Stott, T.E.Stringer, D.Stubberfield, T.Sugie[18], D.Summers, H.Summers[20], J.Taboda-Duarte[22], J.Tagle[30], H.Tamnen, A.Tanga, A.Taroni, C.Tebaldi[23], A.Tesini, P.R.Thomas, E.Thompson, K.Thomsen[11], P.Trevalion, M.Tschudin, B.Tubbing, K.Uchino[29], E.Usselmann, H.van der Beken, M.von Hellermann, T.Wade, C.Walker, B.A.Wallander, M.Walravens, K.Walter, D.Ward, M.L.Watkins, J.Wesson, D.H.Wheeler, J.Wilks, U.Willen[12], D.Wilson, T.Winkel, C.Woodward, M.Wykes, I.D.Young, L.Zannelli, M.Zarnstorff[6], D.Zasche[14], J.W.Zwart.

PERMANENT ADDRESS

1. UKAEA, Harwell, Oxon. UK.
2. EUR-EB Association, LPP-ERM/KMS, B-1040 Brussels, Belgium.
3. Institute National des Récherches Scientifique, Quebec, Canada.
4. ENEA-CENTRO Di Frascati, I-00044 Frascati, Roma, Italy.
5. Chalmers University of Technology, Göteborg, Sweden.
6. Princeton Plasma Physics Laboratory, New Jersey, USA.
7. UKAEA Culham Laboratory, Abingdon, Oxon. UK.
8. Plasma Physics Laboratory, Space Research Institute, Sao José dos Campos, Brazil.
9. Institute of Mathematics, University of Oxford, UK.
10. CRPP/EPFL, 21 Avenue des Bains, CH-1007 Lausanne, Switzerland.
11. Risø National Laboratory, DK-4000 Roskilde, Denmark.
12. Swedish Energy Research Commission, S-10072 Stockholm, Sweden.
13. Imperial College of Science and Technology, University of London, UK.
14. Max Planck Institut für Plasmaphysik, D-8046 Garching bei München, FRG.
15. Institute for Plasma Research, Gandhinagar Bhat Gujat, India.
16. FOM Instituut voor Plasmafysica, 3430 Be Nieuwegein, The Netherlands.
17. Commissiariat à L'Energie Atomique, F-92260 Fontenay-aux-Roses, France.
18. JAERI, Tokai Research Establishment, Tokai-Mura, Naka-Gun, Japan.
19. Institute for Aerospace Studies, University of Toronto, Downsview, Ontario, Canada.
20. University of Strathclyde, Glasgow, G4 ONG, U.K.
21. Nuclear Engineering Laboratory, Lapeenranta University, Finland.
22. JNICT, Lisboa, Portugal.
23. Department of Mathematics, Univeristy of Bologna, Italy.
24. Oak Ridge National Laboratory, Oak Ridge, Tenn., USA.
25. G.A. Technologies, San Diego, California, USA.
26. Institute for Nuclear Studies, Swierk, Poland.
27. Commissiariat à l'Energie Atomique, Cadarache, France.
28. School of Physical Sciences, Flinders University of South Australia, South Australia SO42.
29. Kyushi University, Kasagu Fukuoka, Japan.
30. Centro de Investigaciones Energeticas Medioambientales y Techalogicas, Spain.
31. University of Maryland, College Park, Maryland, USA.
32. University of Essex, Colchester, UK.
33. Akademie de Wissenschaften, Berlin, DDR.

CR 88.49.1A